Research
Environmental Protection—Article

MoS$_2$/ZIF-8 Hybrid Materials for Environmental Catalysis: Solar-Driven Antibiotic-Degradation Engineering

Wen-Qian Chen [a,c,#], Lin-Yue Li [a,b,#], Lin Li [a], Wen-Hui Qiu [d,e], Liang Tang [a,b,*], Ling Xu [a], Ke-Jun Xu [a], Ming-Hong Wu [a,b,*]

[a] School of Environmental and Chemical Engineering, Shanghai University, Shanghai 200444, China
[b] Key Laboratory of Organic Compound Pollution Control Engineering, Ministry of Education, Shanghai 200444, China
[c] Shanghai Institute of Applied Radiation, Shanghai University, Shanghai 201800, China
[d] Guangdong Provincial Key Laboratory of Soil and Groundwater Pollution Control, School of Environmental Science and Engineering, Southern University of Science and Technology, Shenzhen 518055, China
[e] State Environmental Protection Key Laboratory of Integrated Surface Water-Groundwater Pollution Control, School of Environmental Science and Engineering, Southern University of Science and Technology, Shenzhen 518055, China

ARTICLE INFO

ABSTRACT

Photocatalytic water purification is an efficient environmental protection method that can be used to eliminate toxic and harmful substances from industrial effluents. However, the TiO$_2$-based catalysts currently in use absorb only a small portion of the solar spectrum in the ultraviolet (UV) region, resulting in lower efficiency. In this paper, we demonstrate a molybdenum disulfide/zeolitic imidazolate framework-8 (MoS$_2$/ZIF-8) composite photocatalyst that increases the photocatalytic degradation of ciprofloxacin (CIP) and tetracycline hydrochloride (TC) by factors of 1.21 and 1.07, respectively. The transformation products of CIP and TC from the catalysis processes are tentatively identified, with the metal–organic framework (MOF) being considered to be the main active species with holes being considered as the main active species. The hydrogen production rate of the MoS$_2$/ZIF-8 nanocomposites is 1.79 times higher than that of MoS$_2$. This work provides a novel perspective for exploring original and efficient 1T/2H-MoS$_2$/MOF-based photocatalysts by optimizing the construction of surface nano-heterojunction structures. The composite photocatalyst is found to be durable, with its catalytic performance being preserved under stability testing. Thus, 1T/2H-MoS$_2$/MOF-based photocatalysts have excellent prospects for practical antibiotic-degradation engineering.

1. Introduction

Given the current global awareness of and attention to environmental pollution, the demand for new environmental-restoration technologies is increasing in many areas, including water pollution. One serious water pollution concern involves the abuse of a large number of broad-spectrum antibiotics, including ciprofloxacin (CIP) and tetracycline hydrochloride (TC), which end up in the water supply. Antibiotics pollution in water is known to be a major issue for human health [1–3]. Over the past few years, various technologies to reduce antibiotics emission have been employed in environmental protection; these include physical adsorption [4,5], microbial degradation [6], and photocatalytic degradation [7]. Among these, semiconductor-based photocatalysis is considered to be an effective solution for antibiotics pollution in water due to its environmental friendliness, low energy consumption, and low cost [8,9]. However, in comparison with pollutants such as dyes, it is relatively difficult to photodegrade antibiotics [10,11]. Therefore, there is a great need for the development of new effective photocatalysts with higher antibiotic-degradation efficiency.

Molybdenum disulfide (MoS$_2$) is a transition metal dichalcogenide catalyst with a structure that is similar to a two-dimensional (2D) graphene analog layered structure that has been attracting a great deal of attention in the catalysis of antibiotic degradation [12,13]. The S—Mo—S coordination in the lattice is similar to a "sandwich" structure, and produces an unsaturated

phenomenon at the edges [14]. In addition, MoS_2 has a tunable band gap structure, which varies from an indirect band gap of 1.2 eV (for bulk MoS_2) to an indirect band gap of 1.8 eV (for monolayer MoS_2) [15,16]. However, the limitations of its narrow band gap and specific surface area impede the catalytic activity of MoS_2. Therefore, MoS_2 has been constructed into different morphologies in order to improve its catalytic performances, including nanosheets, nanoparticles, and quantum dots. MoS_2 has two common phases [17]: the metallic $1T-MoS_2$, with more catalytically active sites, and the semiconducting $2H-MoS_2$, with more active edge zones. It is necessary to synthesize mixed-phase MoS_2 with many active edge sites in order to maximize the photocatalytic activity of this catalyst.

A metal–organic framework (MOF) is a kind of crystalline material with high porosity and a huge surface area, which has shown varying degrees of potential in catalysis application [18,19]. Zeolitic imidazolate framework-8 (ZIF-8) is a typical member of the MOF family that consists of zinc (Zn) ions and imidazole linkers. ZIF-8 has been widely studied due to its high specific surface area, excellent thermal/chemical stability, and carbon dioxide (CO_2) affinity [20,21]. Thus, it is assumed that the combination of ZIF-8 nanocrystals with MoS_2 nanosheets will greatly increase the specific surface area, adsorption, and number of photocatalytic reaction sites, thereby improving the photocatalytic degradation efficiency of the entire photocatalyst. In this work, we demonstrate that ZIF-8 being tightly anchored on the $1T/2H-MoS_2$ nanosheets. In terms of catalytic performance, the composite catalyst shows greater photocatalytic antibiotic degradation activity than MoS_2 on its own.

2. Experiments

2.1. Preparation of ZIF-8 nanocrystals

The ZIF-8 was synthesized according to previously published procedures [22]. In general, 1.81 g of zinc nitrate hexahydrate ($Zn(NO_3)_2 \cdot 6H_2O$) was dissolved in 10 mL of deionized (DI) water; 1.0 g of 2-methylimidazole (2-MeIm, AR) was then dissolved in 10 mL of ammonia solution ($NH_3 \cdot H_2O$, AR). Next, the 2-MeIm solution was slowly added in a drop-wise manner to the zinc nitrate solution, which was magnetically stirred at room temperature for 8 h. The final product was subsequently centrifuged and washed to neutrality. Finally, the white ZIF-8 nanocrystal was obtained after freeze-drying for 12 h.

2.2. Preparation of $1T/2H-MoS_2$/ZIF-8 composite

$1T/2H-MoS_2$/ZIF-8 was prepared by a solvothermal method. In brief, 0.151 g (2 mmol) thioacetamide (TAA, AR $\geq$ 99.0%), 0.242 g (1 mmol) sodium molybdate (Na_2MoO_4, AR $\geq$ 99.0%), and 0.05 g (0.14 mmol) cetyltrimethyl ammonium bromide (CTAB, AR) were dissolved in 10 mL DI water, which was stirred for 5 min to obtain a homogeneous solution. An amount of ZIF-8 (a mass of 8.0, 11.2, 16.0, 24.0, or 32.0 mg) was then added to the mixed solution. Subsequently, 40 mL of N,N-dimethylformamide (DMF, AR $\geq$ 99.5%) was added to the mixed solution. After sonicating for 2 h, the mixed solution was transferred into a Teflon autoclave and kept in an oven at 200 °C for 24 h. The final black product was centrifuged at 8000 r·min^{-1} and washed with 75 vol% ethanol. Finally, the prepared black product was freeze-dried for 24 h. The samples were marked as MZ-5, MZ-7, MZ-10, MZ-15, and MZ-20, where MZ refers to the MoS_2/ZIF-8 composite and the numbers refer to the weight content of ZIF-8 (i.e., 5%, 7%, 10%, 15%, and 20%, respectively). The schematic synthesis procedure is shown in Fig. 1. Pure

MoS_2 was synthesized by a similar solvothermal method without the addition of ZIF-8.

2.3. Characterization of $1T/2H-MoS_2$/ZIF-8

The phase structure of these samples was determined using D8 ADVANCED powder X-ray diffraction (XRD, Bruker Corporation, Germany). The microstructures and components of the as-prepared products were determined using a JEM-2010F transmission electron microscope (TEM, JEOL Ltd., Japan) and a FESEM-4800 scanning electronic microscope (SEM, Hitachi Ltd., Japan). The ultraviolet–visible light diffuse reflectance spectra (UV–vis DRS) were obtained using an Cary 300 spectrometer (Agilent Technologies, USA). The excitation wavelength of the photoluminescence (PL) spectrum was 365 nm (F-7000 fluorescence spectrophotometer, Hitachi Ltd., Japan).

2.4. Photocatalytic activity measurements

The photocatalytic degradation of aqueous solutions of CIP (purity $\geq$ 98.0%, 20 mg·L^{-1}) and TC (purity $\geq$ 98.0%, 20 mg·L^{-1}) was performed on $1T/2H-MoS_2$/ZIF-8 composites under visible light irradiation. A 300 W xenon (Xe) lamp (Nanjing Sidongke Electrical Equipment Co., China) with a 420 nm cut-off filter was used as a natural light source. In each test, a 20 mg sample of catalyst and 50 mL of the target pollutant (dissolved in water) were mixed in a quartz tube. Before irradiation, the solution was stirred for 30 min under dark conditions. During irradiation, 2 mL of the mixed solution was taken out of the reactor and filtered with a 0.45 μm needle filter. The absorbance peaks for CIP (276 nm) and TC (357 nm) were measured using a TU-1810 spectrophotometer (PERSEE Ltd., China) [23,24]. The photocatalytic hydrogen (H_2) evolution reactions were performed in an airtight quartz reactor with cooling water in order to maintain the reaction temperature at 25 °C; a 500 W Xe lamp was used as a natural light source. Prior to irradiation, 25 mg of photocatalyst powder was dispersed in 50 mL of 15 vol% triethanolamine (TEOA, AR) aqueous solution. During irradiation, H_2 was detected by a gas chromatograph (GC7920, Beijing CEAULIGHT Co. Ltd., China) with nitrogen (N_2) as the carrier gas. The area of the integrated peak of the gas chromatography (GC) curve was compared with the area of the integral peak of the standard H_2 curve at a certain volume; the actual amount of H_2 was then calculated. The degradation intermediates were detected by means of high-performance liquid chromatography–tandem mass spectrometry (LC–MS/MS, 6460 Triple Quad LC–MS/MS, Agilent). Detailed analysis methods for the degradation products are provided in Appendix A.

2.5. Photoelectrochemical performance

Transient photocurrent electrochemical impedance spectroscopy (EIS) and Mott–Schottky plots were conducted on an electrochemical analyzer (CHI660E electrochemical workstation, Chenhua Instrument, Shanghai, China). The as-synthesized samples were used as the working electrode, while a saturated calomel electrode (SCE) and a platinum sheet were used as the reference electrode and counter electrode, respectively. Detailed methods for the preparation of photoelectrodes are reported in the literature [25]. A 500 W Xe arc lamp with a 420 nm cut-off filter was used as a light source. The Mott–Schottky tests were implemented using the impedance-potential mode. EIS tests were performed at an open-circuit potential in a frequency range between 10^5 and 10^{-2} Hz in a dark environment. In all experiments, 0.5 mol·L^{-1} Na_2SO_4 aqueous solution was used as the electrolyte.
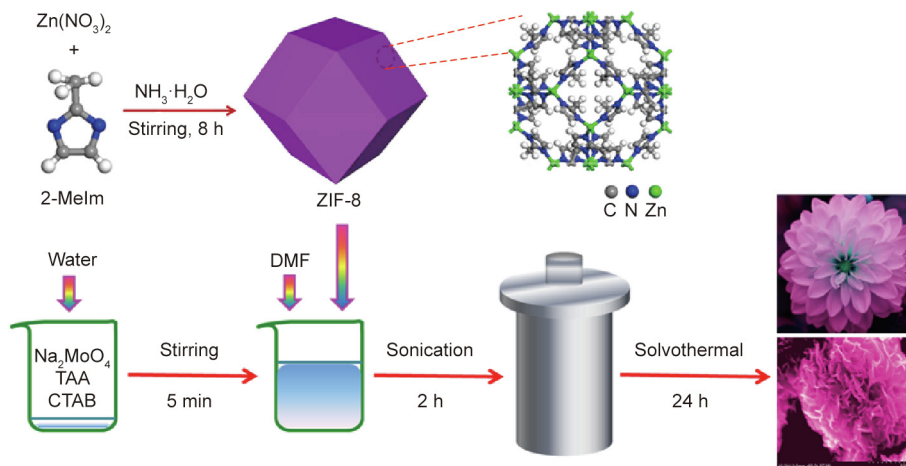
Fig. 1. A schematic illustration of the preparation of MZ nanocomposites.

3. Results and discussion

3.1. Microstructures and components

The crystallinity of MoS_2 and of the 1T/2H-MoS_2/ZIF-8 nanocomposites was investigated by XRD; measurement results are displayed in Fig. 2. The XRD pattern of the synthesized MoS_2 was different from that of pristine 2H-MoS_2, as new (002) and second (002)* diffraction peaks of the as-synthesized MoS_2 showed at 9.6° and 18.0°, respectively [26]. According to the Bragg equation, the lattice spacing of the (002) plane was calculated to be 0.95 nm (Fig. 3(e)), which aligned with the interlayer distance from the TEM images. The increase in the interlayer distance of the MoS_2 indirectly indicated that the prepared MoS_2 was a metallic 1T phase [27]. Fig. 3(f) shows that a fringe spacing of 0.27 nm can indicate the (100) crystal plane index of 2H-MoS_2. As indicated by Fig. S1(a), it is evident that in comparison with the standard value (JCPDS Card No. 37-1492), the two diffraction peaks at 32.7° and 58.4° respectively indicate the (100) and (110) planes. The results indicate that the local atomic arrangement remains the same as that of the standard 2H-MoS_2 structure [28], which confirms that the prepared MoS_2 is a polytype phase. In addition, it can be seen from Fig. S1(b) that the MZ-20 nanocomposite contains ZIF-8 crystal, which signifies that the ZIF-8 is in close contact with the MoS_2 nanosheets. Fourier transform infrared (FT-IR) spectroscopy of the MZ-7 and ZIF-8 are shown in Fig. 4. The presence of ZIF-8 is revealed by the following characteristic peaks: the band at 421 cm^{-1} is attributed to the Zn—N stretch, and other bands in the spectral region of 500–1500 cm^{-1} are due to plane bending and stretching of the imidazole ring [29]. It is worth noting that the same adsorption bands were observed for the MZ-7 nanomaterial. For MZ nanomaterials, it can be seen that the characteristic peaks are consistent with those of pure MoS_2 (Fig. S2), which confirms that the metal-phase MoS_2 was successfully prepared.

We examined pure MoS_2, MZ-7, and MZ-20 samples by SEM (Fig. S3) and TEM (Fig. 3) to understand the degree of complexation of the ZIF-8 crystals with MoS_2. As shown in Figs. S3(a, b), MZ-7 exhibits a flower-like structure. Furthermore, these lamella flowers are not completely isolated from each other, but are often superimposed together. Small particles of ZIF-8 fit tightly on the flower-like 1T/2H-MoS_2 surface. Careful observation of the morphology of MZ-7 shows that many curled and staggered nanosheets grow densely on the surface. In MZ-20, the flower-like structure gradually disappears, showing a smooth surface covered by ZIF-8. The probable reason for this structural change is that the increasing content of ZIF-8 affects the anisotropic growth and flower-like structure
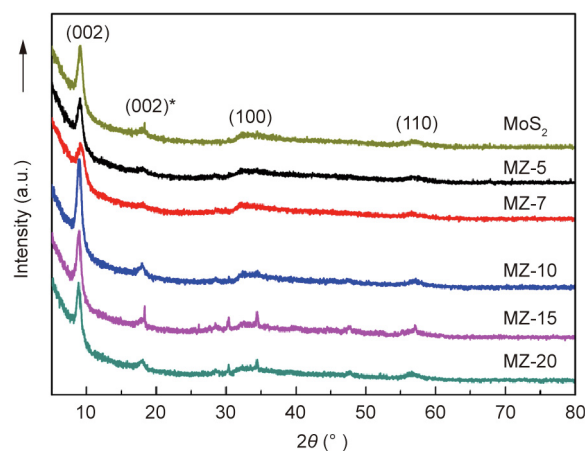

Fig. 2. XRD patterns of MoS_2 and MZ.

formation of the 1T/2H-MoS_2. As indicated in Figs. 3(a–d), which shows TEM images of a single MZ-7 petal nanosheet, the 1T/2H-MoS_2 nanosheets are curled to form tubular structures. ZIF-8 particles are partially attached to the tubular 1T/2H-MoS_2 structures. Under electron beam irradiation, these nanosheets are extremely transparent, which indicates that the sheets are very thin (Figs. 3(b, c)). An ultrathin tubular structure is more conducive to the rapid transmission of photo-induced electrons, and thus reduces the recombination rate. Fig. 5 shows the presence of the elements sulfur (S), molybdenum (Mo), Zn, nitrogen (N), and carbon (C) in the MZ-7 nanocomposite. It is notable that these elements are uniformly distributed throughout the MZ-7, and it is further confirmed that the ZIF-8 is very uniformly dispersed and attached to the 1T/2H-MoS_2.

The pore characteristics of the as-prepared samples were investigated by the N_2 physical sorption method (Fig. 6). The N_2 adsorption/desorption isotherms of MZ-5, MZ-7, MZ-10, MZ-15, and MZ-20 are type IV adsorption curves (Figs. 6 and S4(a–c)). At higher relative pressures (P/P_0), the MZ-7 sample exhibits higher adsorption performance compared with other prepared samples, which reveals the existence of cumulative pores [30]. Unlike the MZ nanocomposites, a distinctive type I isotherm is shown by the ZIF-8 (Fig. S4(d)). The specific surface areas of MZ-5, MZ-7, MZ-10, MZ-15, and MZ-20 were measured to be 17.789, 33.308, 25.150, 11.482, and 27.354 $m^2 \cdot g^{-1}$, respectively (Table S1). These findings show that MZ-7 provides more adsorption and
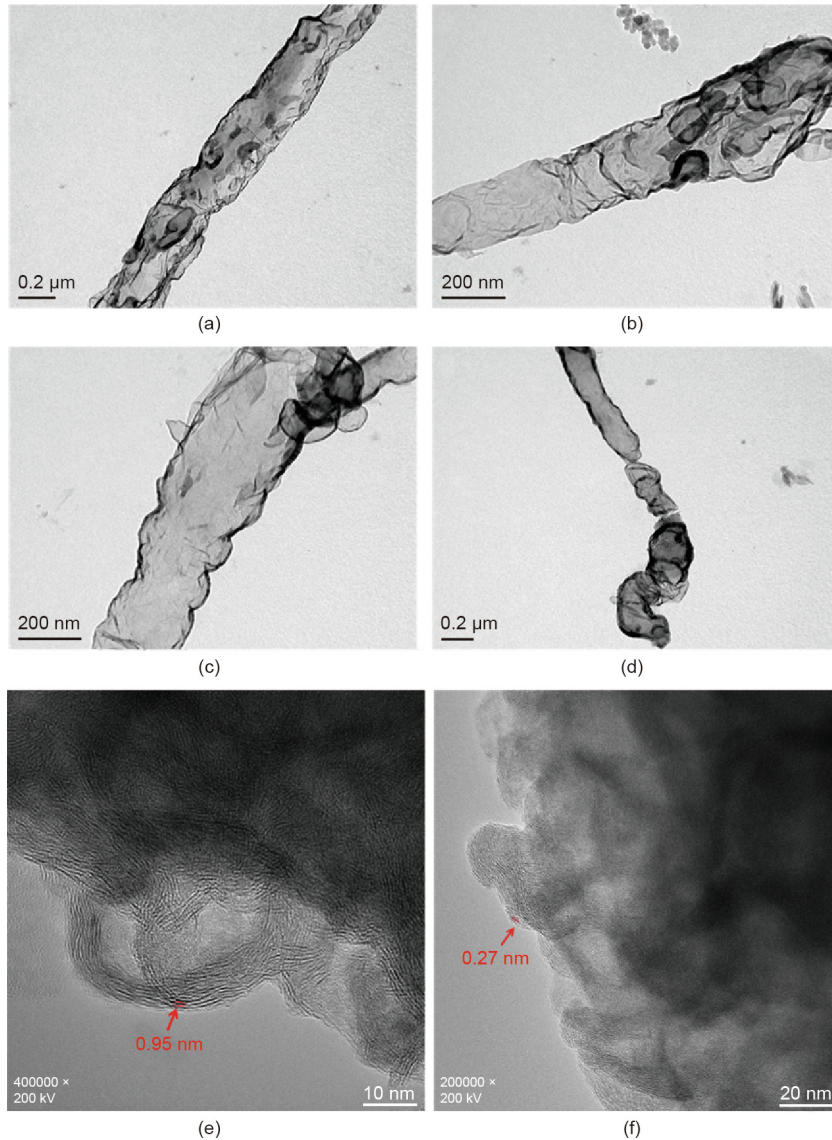
Fig. 3. (a–d) TEM images and (e, f) high-magnification TEM images of the MZ-7 nanocomposites.
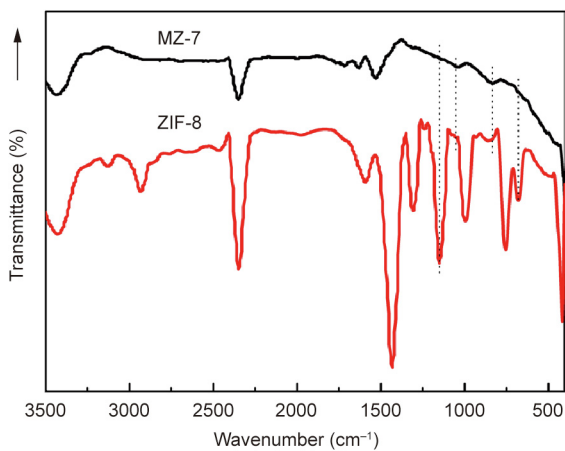
Fig. 4. FT-IR spectra of MZ-7 and ZIF-8.

photocatalytic active sites than the other nanocomposites. In addition, as shown in the inset of Fig. 6(a), MZ-7 mainly contains mesoporous types (2–8 nm) corresponding to the Barrett–Joyner–Halenda pore-size distribution curve. Furthermore, the pore-size distribution curve of MZ-20 shows that the main pore-size range is 1–6 nm (inset Fig. 6(b)). This may be because the addition of ZIF-8 affects the particle size of $1T/2H-MoS_2$. The synergistic effect of its various pores and the high specific surface area of MZ-7 are conducive to the rapid mass transfer of the target contaminant molecules and diffusion of photo-induced electrons [31]; thus, MZ-7 is expected to display excellent photocatalytic degradation.

The elemental composition and functional characterization of the $1T/2H-MoS_2/ZIF-8$ nanomaterials were further confirmed by X-ray photoelectron spectroscopy (XPS). In Fig. 7(a), the XPS survey spectrum shows that MZ-7 mainly consists of the elements S, Mo, Zn, C, and N. The XPS results of S 2p are displayed in Fig. 7(b). The MZ-7 has three peaks at 163.8, 162.4, and 160.9 eV that can be assigned to S $2p_{1/2}$ and S $2p_{3/2}$ [32]. As shown in Fig. 7(c), the Mo 3d binding energy spectrum of MZ-7 has four peaks at 235.0, 231.7, 228.1, and 225.3 eV, which corroborate the presence of Mo $3d_{5/2}$ and $3d_{3/2}$ [23]. When the S 2p and Mo 3d spectra of MZ-7 and MoS_2 are compared, the result indicates that the S 2p and Mo 3d spectra of MZ-7 shift to higher binding energies by 0.7 eV, which satisfies the previously observed relaxation energy before the formation of $1T-MoS_2$. A significant increase in binding energy
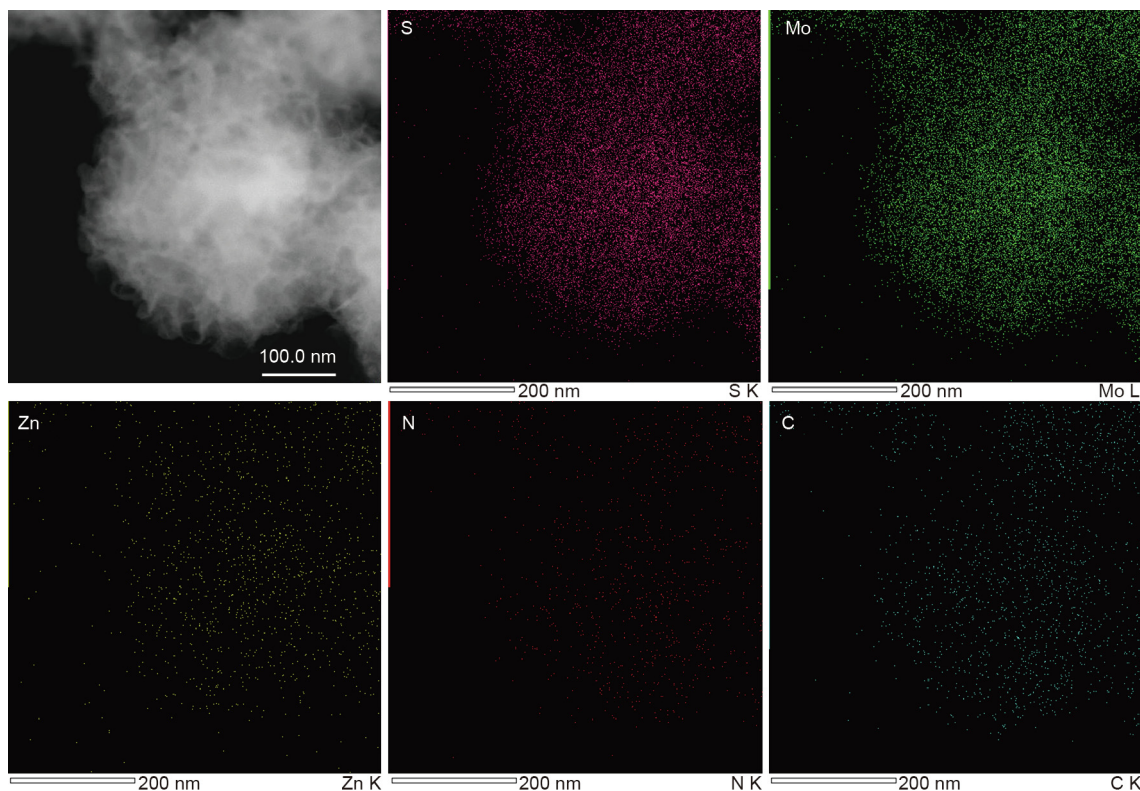
Fig. 5. Energy-dispersive spectroscopy (EDS) elemental mappings of the obtained MZ-7 nanocomposites.
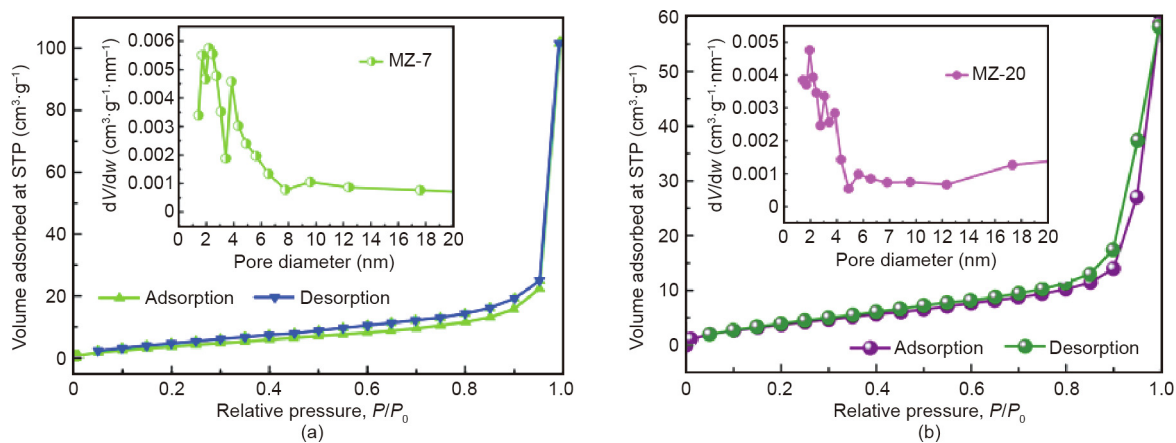

Fig. 6. N_2 sorption isotherms and pore-size distribution of the (a) MZ-7 and (b) MZ-20 composites. STP: standard temperature and pressure.

of 0.70 eV usually indicates a loss of electron density [33], which can generate more active vacancies and thus increase the photocatalytic effect. As illustrated in Figs. 7(d–f), the results suggest that the composite MZ-7, which includes ZIF-8, contains the elements Zn, C, and N. Two peaks are observed at 1044.0 eV (Zn 2p1/2) and 1020.9 eV (Zn 2p3/2), respectively, which correspond to the Zn^{2+} of the ZIF-8 (Fig. 7(d)). As a comparison, the Zn 2p peaks of ZIF-8 are located at 1044.7 eV and 1021.6 eV. MZ-7 shows a negative shift of 0.7 eV relative to ZIF-8, which may be due to electron transfer [34]. In the C 1s XPS spectrum (Fig. 7(e)), three binding energies of MZ-7 peak at 288.5, 285.9, and 284.5 eV; these can be assigned to the carboxyl carbon (O=C—O), hydroxyl carbon (C—O), and sp²-hybridized carbon (C—C) [35]. In Fig. 7(f), the N 1s band peaks are 398.8, 397.0, and 394.5 eV; these can be attributed to the C—N bond and the 2-methylimidazole nitrogen atoms

[36]. The XPS results reveal that MoS_2 fits snugly on the ZIF-8 surface, and that specific elements are prominently present in the composite. It is evident that the positions of the S 2p, Mo 3d, and Zn 2p peaks in MoS_2/ZIF-8 are shifted a little, indicating that the MoS_2 and ZIF-8 are interacting with each other. It is likely that the ZIF-8 nanocrystals become embedded in the MoS_2 nanosheets during the solvent heat treatment [37]. Thus, the above analyses indicate that 1T/2H-MoS_2 was successfully synthesized in this work. More importantly, the results suggest that the prepared samples have more active sites and more significant photocatalytic effects than MoS_2 or ZIF-8 on their own.

The absorbance performance of the MZ nanocomposites and MoS_2 was measured using UV–vis DRS. Fig. 8(a) shows that all samples display significantly enhanced light absorption between 200 and 800 nm. The characteristic absorption for pure ZIF-8 is
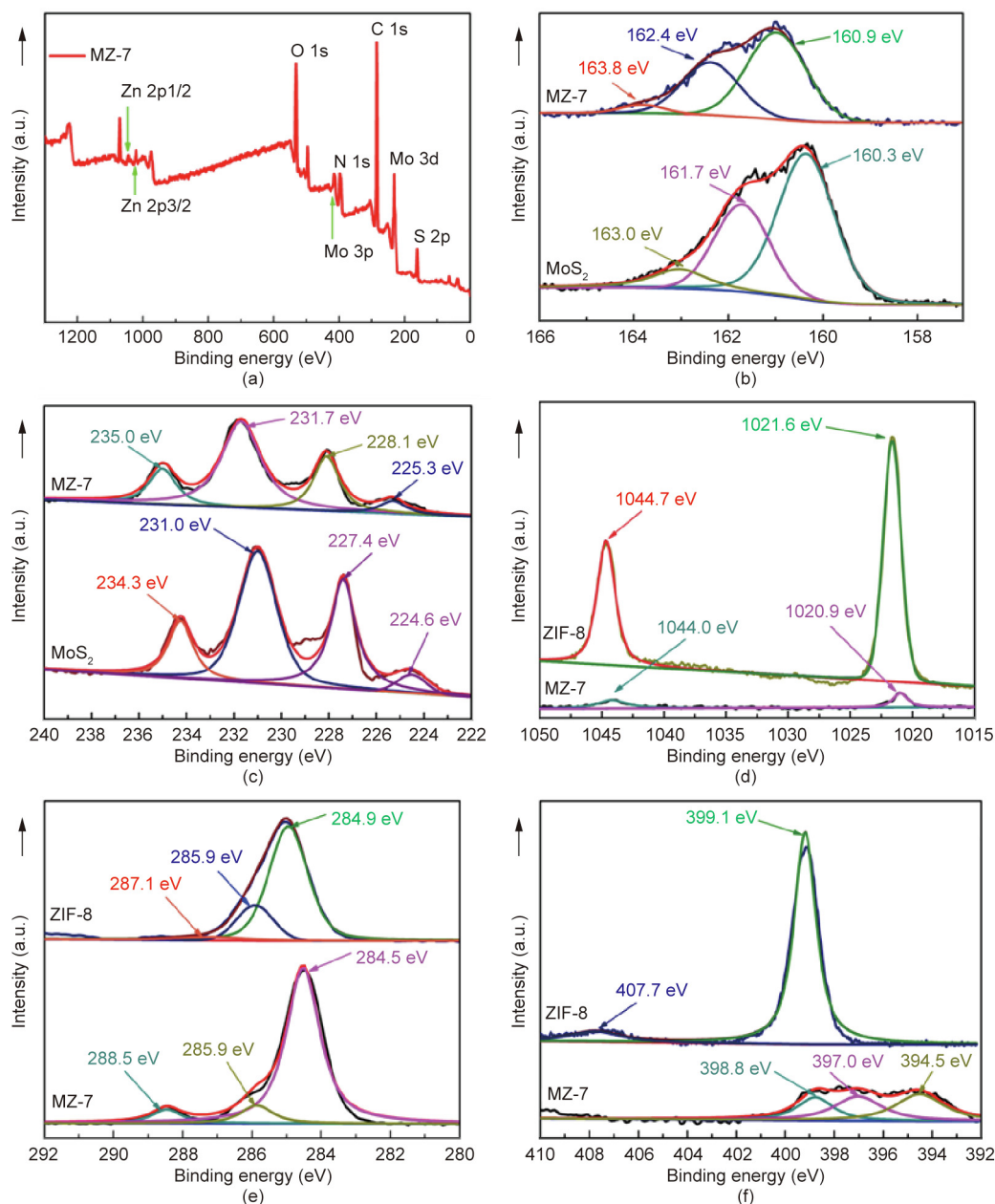
Fig. 7. XPS spectra of MZ-7 compared with pure MoS$_2$ and ZIF-8. (a) Survey scan; (b) S 2p; (c) Mo 3d; (d) Zn 2p; (e) C 1s; (f) N 1s.

detected at around 225 nm (Fig. S5(a)). However, when ZIF-8 is loaded with 1T/2H-MoS$_2$, the light absorption capacity is significantly improved, indicating the importance of the hybrid composite in enhancing photocatalysis. This finding means that the higher visible light absorption of the heterojunction between ZIF-8 and 1T/2H-MoS$_2$ leads to the photogeneration of electron-hole pairs, which further promote the photocatalytic performance. The relationship between the wavelength of different nanocomposites and the photon energy (eV) can be calculated by the Kubelka–Munk function (K–M function), provided below [38]:

$$F(R) = \frac{(1 - R)^2}{2R} \tag{1}$$

where R is the reflectance and $F(R)$ is proportional to the absorption coefficient (α).

The relationship between the K–M function and the wavelength of all the synthesized composites is shown in Fig. 8(b). As shown in

Figs. 8(c, d), the band gap energies (E_g) of 1T/2H-MoS$_2$ and ZIF-8 are estimated from the tangent to the curve of $(\alpha h \nu)^{1/2}$ (or $(\alpha h \nu)^2$) with respect to the photo-energy. The band gaps of 1T/2H-MoS$_2$, ZIF-8, and MZ-7 (Fig. S5(b)) are 1.13, 5.12, and 1.05 eV, respectively, indicating that the introduction of 1T/2H-MoS$_2$ reduced the band gaps. All the results suggest that the visible light response of the sample is increased; it can now generate more photogenerated carriers to improve the photocatalytic performance.

3.2. Photocatalytic properties

To assess the potential use of the MZ samples in environmental remediation, their photocatalytic activities were evaluated in terms of the photocatalytic degradation of CIP and TC. As can be observed from Fig. 9(a), all samples exhibit catalytic properties in the degradation of CIP. Among the samples, MZ-7 has the highest catalytic efficiency, which is in agreement with the Brunauer–
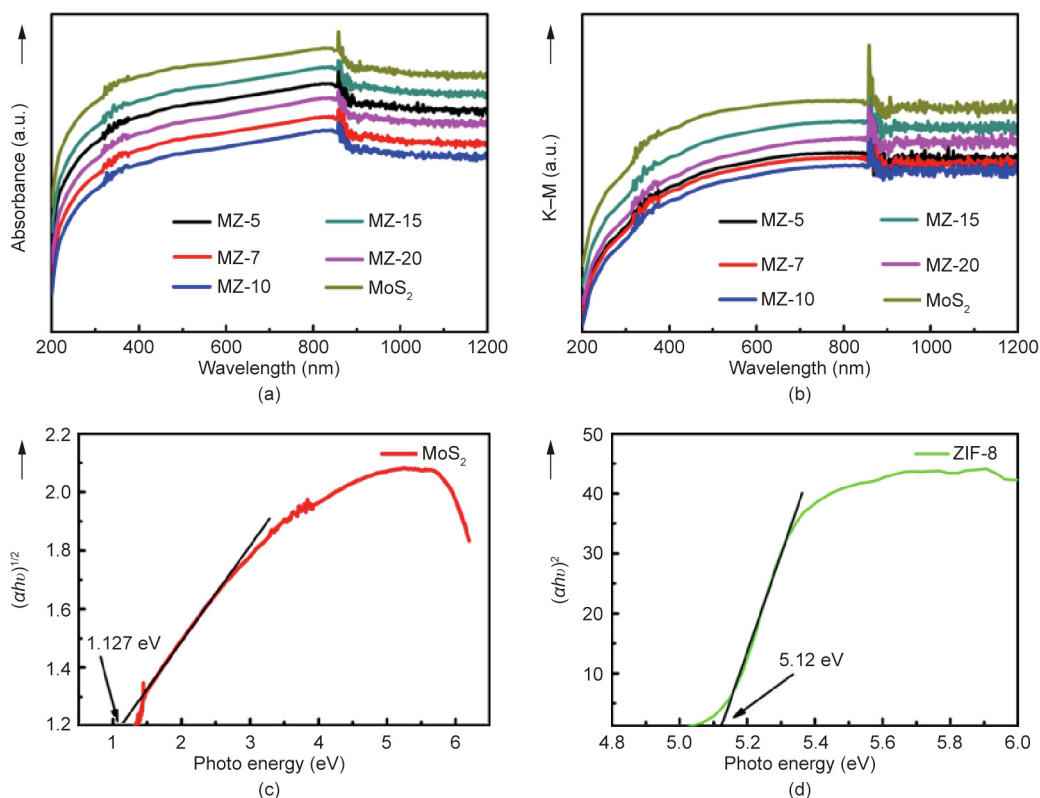
Fig. 8. (a) UV–vis DRS spectra of MZ nanocomposites and pure MoS_2; (b) plot of K–M function estimated from UV–vis DRS spectra of MZ nanocomposites; (c) plot of $(\alpha h\nu)^{1/2}$ vs. photo-energy ($h\nu$) of pure MoS_2; (d) plot of $(\alpha h\nu)^2$ vs. photo-energy ($h\nu$) of ZIF-8.

Emmett–Teller (BET) surface area analysis. As the content of ZIF-8 increases, the catalytic performance of the samples improves at first, and then gradually decreases. After irradiation for 180 min under visible light, the photodegradation rates of CIP by the MZ-7 hybrids increased to 93.2%, which is 1.21 times greater than that of pure MoS_2. Fig. 9(b) depicts the photodegradation kinetics for CIP by the MZ nanocomposites with different amounts of ZIF-8, and by pure MoS_2. The kinetic curve of CIP degradation is in accordance with the pseudo first-order linear transformation $\ln(C/C_0) = -kt$ [39]. Meanwhile, the pseudo first-order reaction kinetics (k) value of MZ-7 (0.0099 min^{-1}) is 1.29 times and 1.71 times higher than those of MZ-20 and pure MoS_2, respectively; this can be attributed to the coupling of the nanostructured sheets and ZIF-8 within the ultrathin structure of 1T/2H-MoS_2, which provides a pathway for the rapid transfer of photogenerated charge carriers. The small amount of CTAB helps 1T/2H-MoS_2 to generate ultrathin nanosheets [40].

It is worth noting that the removal efficiency of TC reaches 75.6% in the presence of the photocatalyst MZ-7 at 180 min under visible light irradiation (Fig. 9(c)). As seen in Fig. 9(d), k for the removal of TC on MZ-7 is 0.0049 min^{-1} (1.53 times greater than that of MZ-15). This can be ascribed to the rapid separation role of the photogenerated charge carriers by the 1T-MoS_2. Another important factor is that the porous ZIF-8 provides more reactive sites and enhances the progress of photocatalytic degradation. Interestingly, the photocatalytic activity can be improved by doping ZIF-8 on the surface of 1T/2H-MoS_2. 1T-MoS_2 has excellent electrical conductivity and accelerates the transmission of photoexcited electrons, while 2H-MoS_2 provides many active attachment sites on the edge. In addition, ZIF-8 increases the specific surface area of MZ-7, giving it more catalytic centers. Moreover, the synergistic effect between 1T/2H-MoS_2 and ZIF-8 plays an important role in the degradation of CIP and TC.

The photocatalytic activities were assessed by photocatalytic hydrogen evolution reaction in TEOA aqueous solution under visible light irradiation ($\lambda \geq 420$ nm). As shown in Fig. S6, the content of ZIF-8 significantly affected the efficiency of hydrogen production. This test indicated that MZ-7 has the greatest photocatalytic activity, with a hydrogen production rate of 61.45 μmol·h^{-1}·g^{-1}, which is 1.79 times greater than that of pure MoS_2. Thus, the test indicated that the addition of an appropriate amount of ZIF-8 improved the catalytic activity of 1T/2H-MoS_2 for hydrogen production, by increasing the conductivity of the material and providing a larger surface of the exposed edges. These findings also explain the improved photocatalytic activity, which is due to the presence of mixed states and induced structural distortions at the boundaries of the MZ-7 [41]. A more rigorous analysis of these results revealed that a good interfacial heterojunction between 1T/2H-MoS_2 and ZIF-8 contributes to an efficient charge transfer and e$^-$–h$^+$ separation.

3.3. Repeatability and stability of the MZ composites

In order to evaluate the application possibilities of this catalyst in the environment, the reusability and stability of MZ-7 were also tested. The target pollutant of the cyclic test was replaced with CIP with a solution concentration of 20 mg·L^{-1}, and the mass of the photocatalyst was 20 mg. As seen in Fig. 10(a), after two cycles of CIP degradation, the removal rate of CIP was still 90% at the 3rd run within 180 min. The photocatalytic activity of MZ-7 did not decrease significantly, which indicates that the MZ-7 photocatalyst has high stability and can be used repeatedly in practical applications. The XRD result showed that the MZ-7 was chemically stable before and after the reaction (Fig. 10(b)).
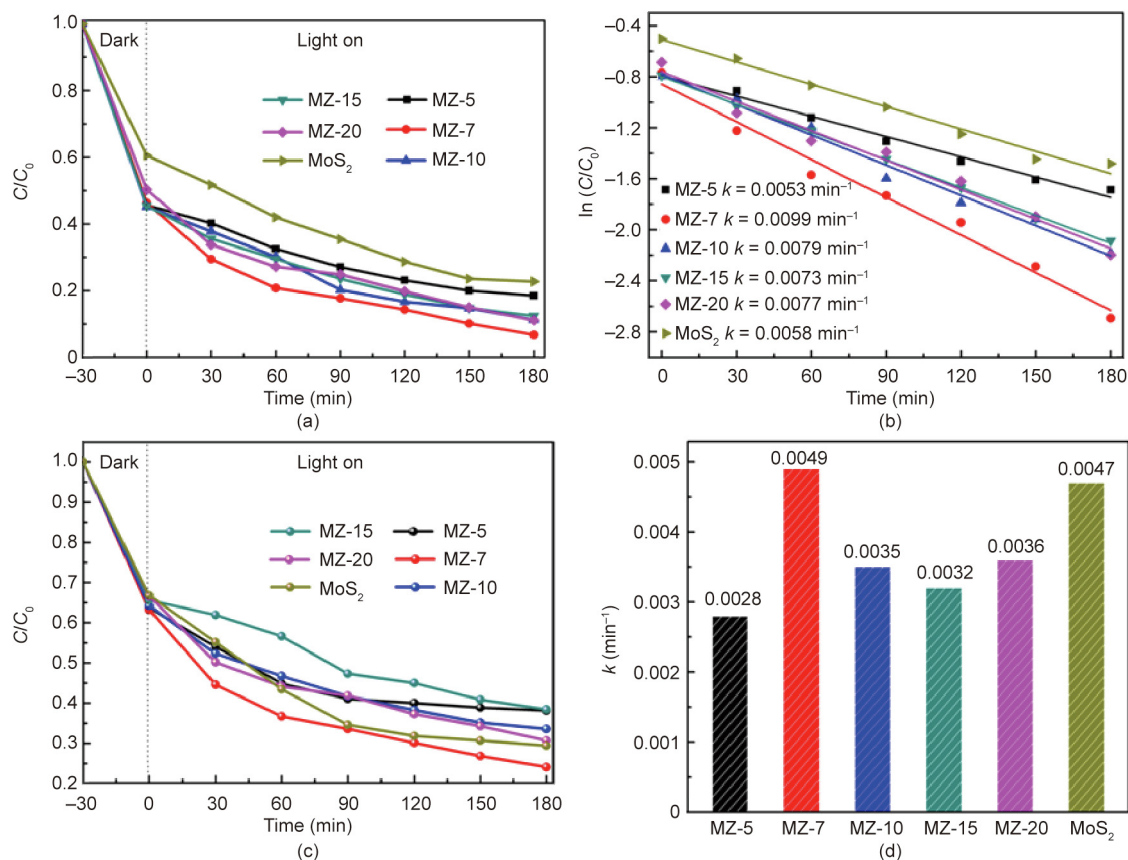
Fig. 9. Photodegradation efficiency and photodegradation rate constants for (a, b) CIP and (c, d) TC by MZ nanomaterials and pure MoS$_2$. C/C_0: normalized concentration.
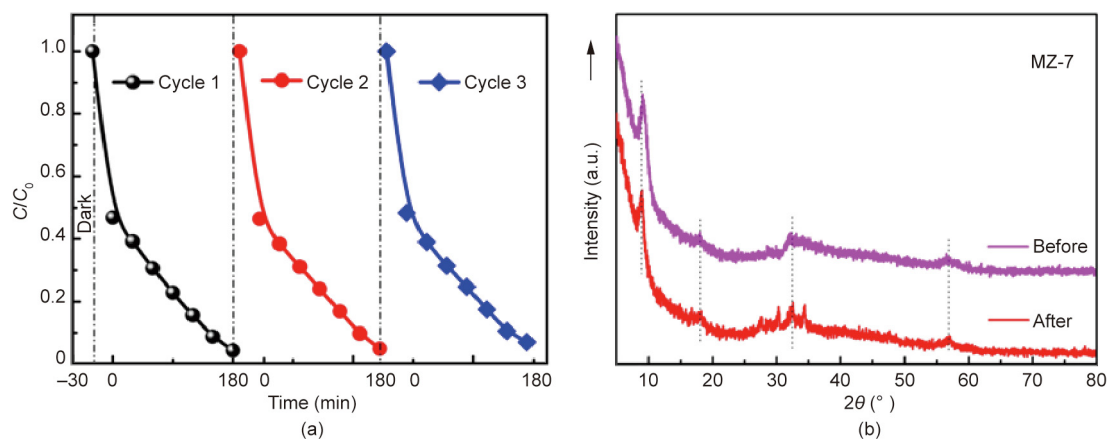

Fig. 10. (a) Recycled performance chart for the MZ-7 composite for CIP; (b) XRD images of the MZ-7 composite before and after the photocatalytic reaction.

3.4. Discussion of the photocatalytic mechanism

Although we obtained a captivating antibiotic-degradation performance with the MZ-7 composite, in order to further clarify the photocatalysis mechanism, radical scavenging experiments were conducted. Three typical scavengers (dosage: 1 mmol·L^{-1})—isopropyl alcohol, EDTA-2Na, and ρ-benzoquinone—were employed as the scavengers of ·OH, h$^+$, and ·O$_2^-$, respectively [42]. For these experiments, the aqueous solution of CIP was 20 mg·L^{-1} and the sample quantity was 20 mg. As shown in Fig. 11(a), the photocatalytic degradation of CIP was significantly inhibited after the addition of EDTA-2Na, implying that h$^+$ plays an active role in

photocatalytic reactions. Furthermore, the photodegradation of CIP was inhibited in the presence of isopropanol, confirming that ·OH plays a minor role in photocatalysis. However, the degradation of CIP after the addition of p-benzoquinone was comparable to the absence of sacrificial agent.

The PL spectra shown in Fig. 11(b) provides information on the separation efficiency of the photo-induced electron–hole (e$^-$–h$^+$) pairs [43]. It is shown that the combination of ZIF-8 and 1T/2H-MoS$_2$ can severely reduce PL intensity, which confirms that the recombination of e$^-$–h$^+$ pairs transferred to the surface of the ZIF-8 is hindered. This result is understandable because the flower-like 1T/2H-MoS$_2$ is more conductive to the rapid transfer
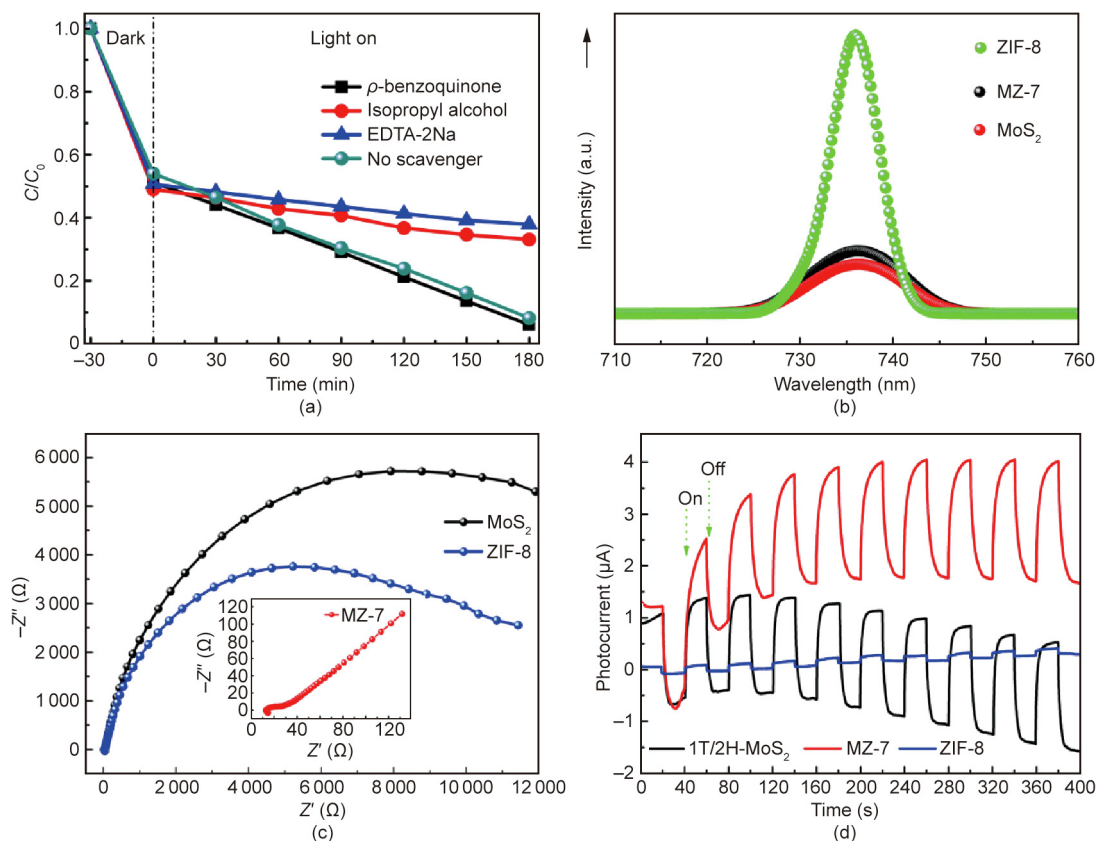
Fig. 11. (a) Influence of different scavengers on the photodegradation of CIP by MZ-7 under visible light irradiation (C_{CIP} = 20 mg·L^{-1}); (b) PL spectra and (c) EIS Nyquist impedance plots of MoS$_2$, ZIF-8, and MZ-7; (d) transient photocurrent responses of 1T/2H-MoS$_2$, MZ-7, and ZIF-8.

of photo-excited electrons through multiple pathways, which reduces the chance of recombination. It is recognized that the surface heterojunction structure between 1T/2H-MoS$_2$ and ZIF-8 can effectively enhance electron–hole migrations, and is thus able to promote photocatalytic performance. To further clarify the above results, the photogenerated charge separation and transfer performance was evaluated by investigating with EIS and photocurrents. As shown in Fig. 11(c), MZ-7 clearly has a smaller arc radius in comparison with pure 1T/2H-MoS$_2$ and ZIF-8 on the EIS Nyquist impedance plot, which confirms that MZ-7 has enhanced photo-induced charge carrier segregation and migration. The EIS Nyquist plots of MZ-5, MZ-7, MZ-10, MZ-15, and MZ-20 are displayed in Fig. S7. A comparison of the arc diameter reveals that the MZ-7 arc radius is smaller than those of the other samples, which indi-

cates effective improvement of the photocarrier transfer and acceleration of charge separation during antibiotic degradation [44]. The heterostructures also contribute to a significant increase in charge transfer efficiency. Fig. 11(d) displays the photocurrent–time curve, which indicates that the photocurrent response of MZ-7 under visible light irradiation is significantly improved in comparison with 1T/2H-MoS$_2$ and ZIF-8. This finding indicates that MZ-7 has the fastest electron-hole pair separation efficiency, which aligns with the aforementioned PL conclusion.

This conclusion is further clarified by the Mott–Schottky measurements. Mott–Schottky measurements were performed to determine the band structure of MZ-7, MoS$_2$, and ZIF-8. All the analysis tests were conducted at 1 kHz frequency in the dark. As shown in Fig. 12(a), the slope of the image indicates that MZ-7 is
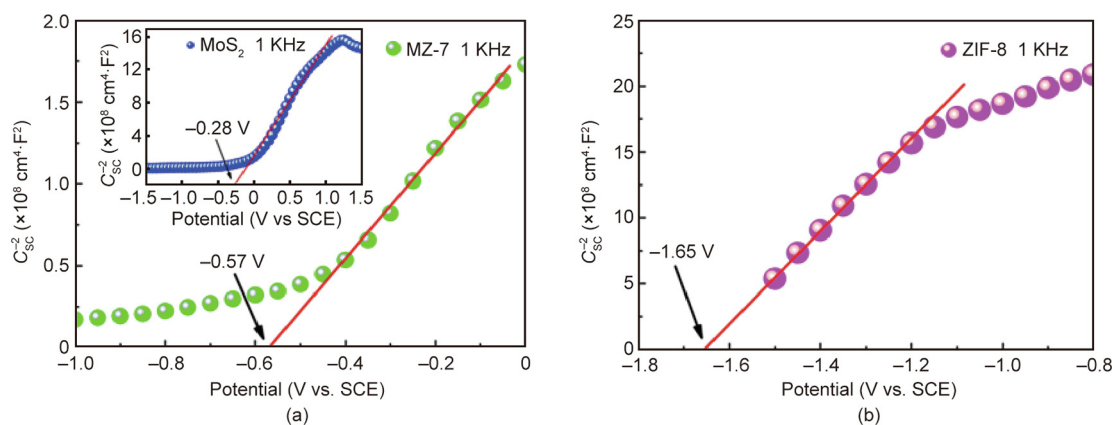
Fig. 12. Mott–Schottky plots of MoS$_2$, MZ-7, and ZIF-8.

a typical *n*-type semiconductor. Its flat band potential is about −0.57 V versus an SCE at pH = 7, which is equivalent to −0.33 V versus the normal hydrogen electrode (NHE) [45]. According to the literature, the bottom of the conduction band (CB) of an *n*-type semiconductor is −0.1 V lower than the flat band potential [46,47]. Therefore, the CB potential of MZ-7 is inferred to be −0.43 V versus NHE, which is lower than the potential of $O_2/\cdot O_2^-$ (−0.33 V versus NHE) [48]. Similarly, the E_{CB} of MoS_2 is inferred to be −0.14 V versus NHE (inset in Fig. 12(a)). As depicted in Fig. 12(b), the E_{CB} of ZIF-8 is calculated to be −1.51 V versus NHE. Taking the UV–vis DRS spectra of MZ-7 into account, the valence band (VB) potential of MZ-7 is computed to be 1.05 V versus NHE, which is lower than $OH^-/\cdot OH$ (1.99 V versus NHE) [49]. This finding indicates that MZ-7 cannot generate •OH radicals by oxidizing OH^- through h^+. However, the holes on the VB of ZIF-8 reacted with hydroxyl groups to obtain •OH. It was found that •OH and $\cdot O_2^-$ are extremely important oxidants for the degradation of antibiotics. Based on the above analysis, it can be further demonstrated that h^+ plays an irreplaceable role in the photocatalytic degradation of TC and CIP. According to UV–vis DRS, the MZ-7 nanocomposite has excellent absorption in visible light. Furthermore, the scavenger testing experiments showed that •OH and h^+ play a pivotal role in photocatalytic degradation. These characterizations indicate that the interaction of MoS_2 and ZIF-8 results

in a composite with outstanding photocatalytic degradation properties. The ultrathin tubular structure of $1T/2H\text{-}MoS_2$ facilitates the capture of photo-excited electrons and ZIF-8 provides more catalytic centers and increases the reaction and adsorption active sites; together, these ensure the photocatalytic degradation capacity of MZ-7.

3.5. Exploration of CIP and TC degradation pathways

In order to further understand the CIP degradation pathway of the MZ-7 nanocomposite, the oxidized products produced via the photocatalytic reaction were detected by liquid chromatography and mass spectrometry (LC–MS). Nine intermediate products were found: P1 (*m/z* = 330), P2 (*m/z* = 304), P3 (*m/z* = 362), P4 (*m/z* = 334), P5 (*m/z* = 291), P6 (*m/z* = 348), P7 (*m/z* = 318), P8 (*m/z* = 261), and P9 (*m/z* = 288). It can be observed that the molecular weight of the intermediate product was lowered, indicating that the CIP was significantly degraded in the MZ-7 reaction system. Based on a combination of these results with the previous literature, we propose three major CIP degradation pathways (i, ii, and iii), shown in Fig. 13. In the first proposed pathway, a hydroxyl group replaces fluorine in CIP, and P1 is first produced after the substitution. Finally, P2, P7, and P8 are formed by epoxidation [50,51]. In pathway ii, the piperazine side chain is oxidatively
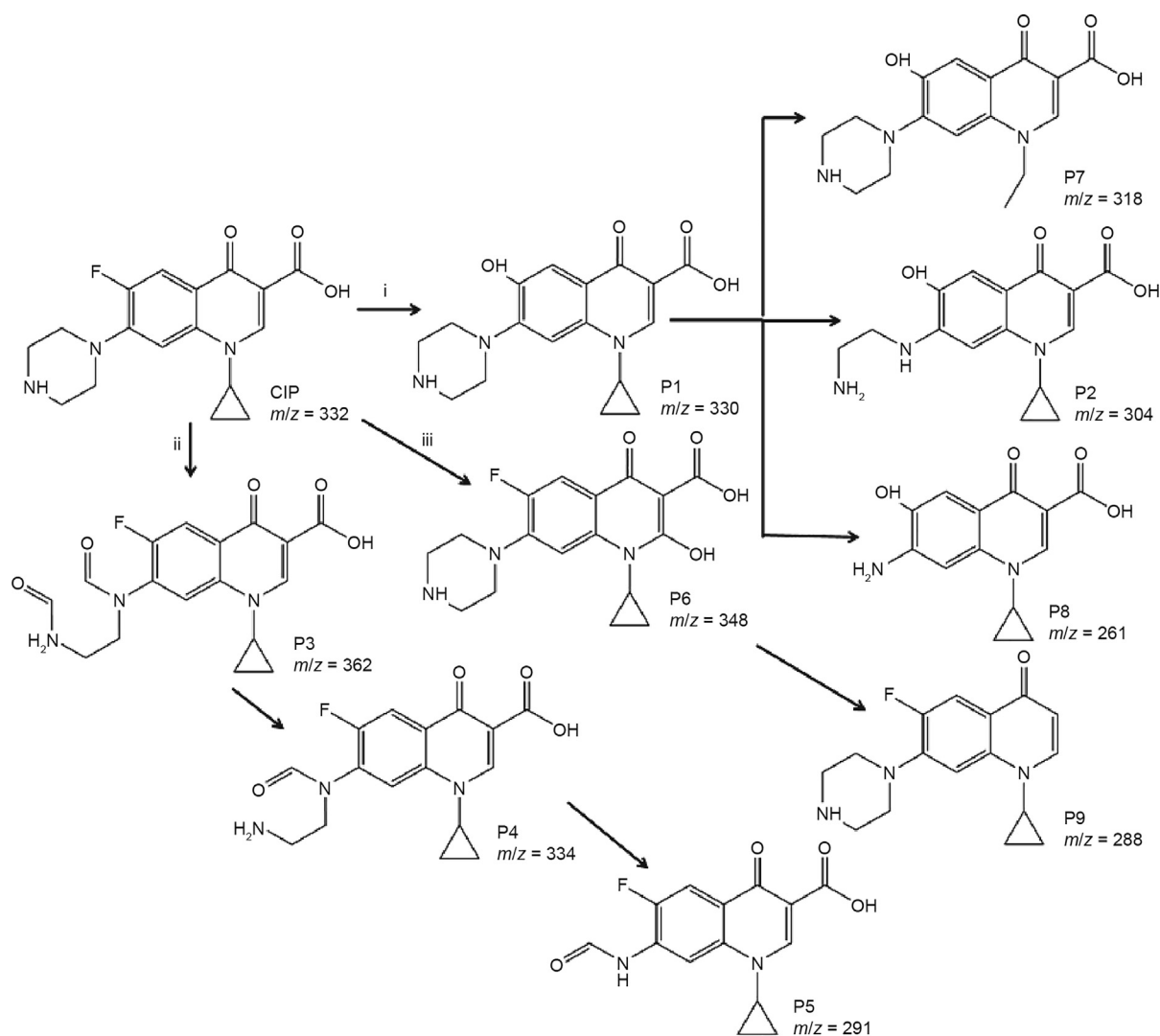

Fig. 13. Proposed degradation pathways for CIP by MZ-7 nanocomposite. *m/z*: mass-to-charge ratio.
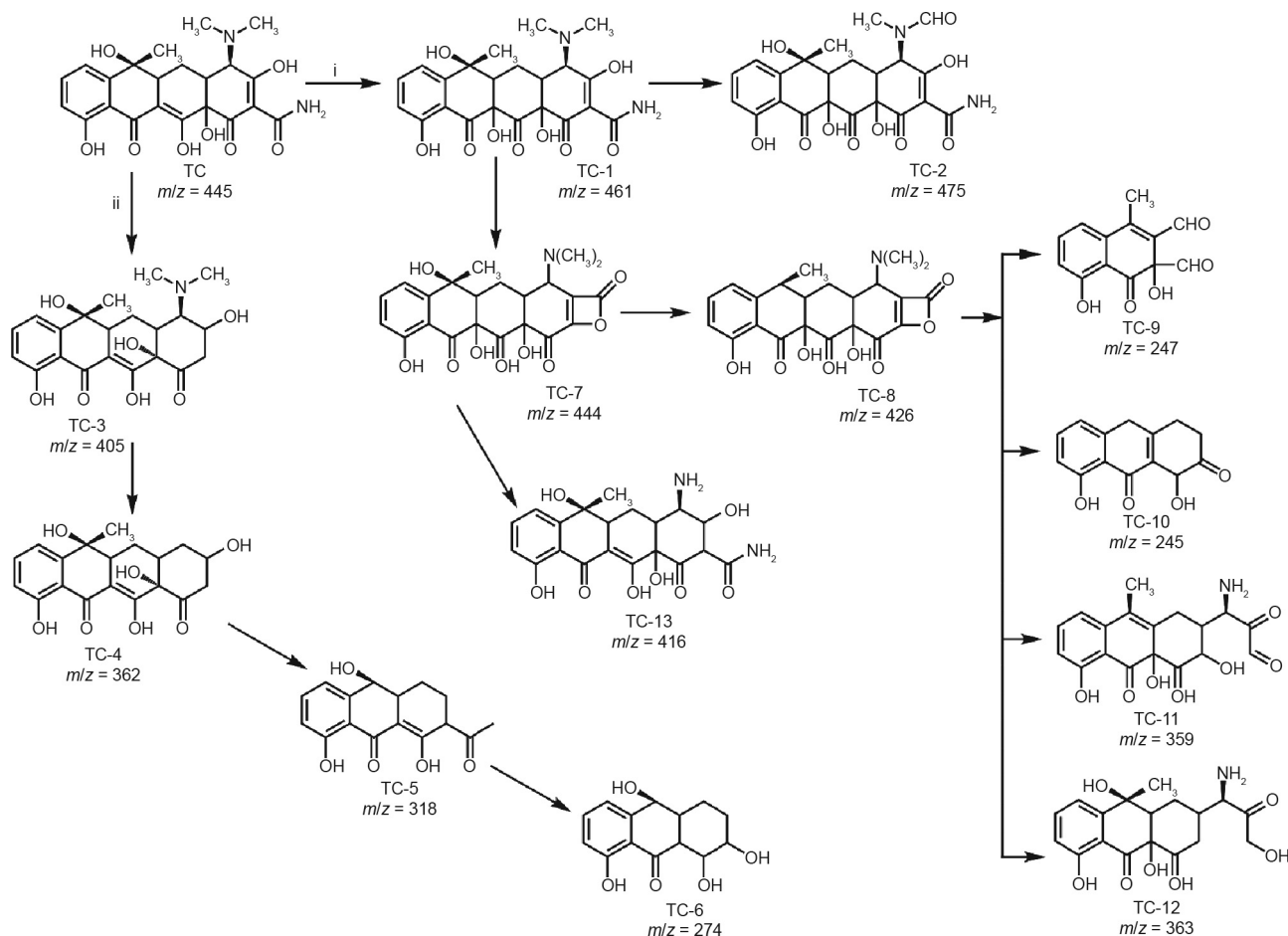
Fig. 14. Proposed transformation pathways for TC degradation by MZ-7 nanocomposite.

degraded, due to the piperazine ring being attacked by ·OH [52,53]. The quinoline epoxidation process in CIP molecules is presented in pathway iii [54,55]. The intermediate product, P6 (m/z = 348), is formed by the combination of CIP and a hydroxyl group. In addition, the intermediate product P9 is formed by the loss of water molecules and carboxyl groups from P6 (m/z = 348). The CIP molecules and intermediates are finally oxidized into smaller molecules including water (H_2O) and CO_2.

The transformation products of TC via photocatalytic degradation were also studied using LC–MS. The possible structures of the products were elucidated based on mass spectrometry. In pathway i (Fig. 14), TC is converted to TC-1 by hydroxylation [56]. Subsequently, an aminomethyl group on TC-1 is attacked by ·OH, resulting in the formation of compound TC-2 [57]. Next, TC-7 is produced through a reaction with the loss of NH_3 at the C=C double-bond with the TC-1. The intermediate TC-7 is transformed to TC-8 via the loss of H_2O. Finally, TC-8 is changed to TC-9, TC-10, TC-11, and TC-12 by oxidation reactions [58]. In pathway ii, TC allows the formation of TC-3 by the removal of –$CONH_2$ and an addition reaction. Simultaneously, TC-3 becomes TC-4 by the loss of –$N(CH_3)_2$ as the irradiation time increases [58,59]. Subsequently, TC-4 is further oxidized and decomposes into TC-6. Finally, the intermediate products are mineralized into other molecules including CO_2 and H_2O.

4. Conclusions

A facile one-pot method has been developed to synthesize highly efficient visible-light-responsive 1T/2H-MoS$_2$/ZIF-8 composites. The photocatalytic activity of MZ-7 in degrading TC and CIP was found to be significantly higher than that of pure MoS_2 exposed to visible light irradiation. It was found that mixed-phase MoS_2 enhances the electron conductivity and increases the density of the active sites, resulting in improved electron transfer and mass transfer efficiency. Moreover, the ultrathin long tubular structure of the MoS_2 contributes to the rapid transport of photo-excited electrons and reduces recombination, thereby enhancing the degradation of TC and CIP. This study provides new insight into the exploration of MOF-based and 1T/2H-MoS$_2$ composite materials for environmental purification and restoration.

Compliance with ethics guidelines

Wen-Qian Chen, Lin-Yue Li, Lin Li, Wen-Hui Qiu, Liang Tang, Ling Xu, Ke-Jun Xu, and Ming-hong Wu declare that they have no conflict of interest or financial conflicts to disclose.

Appendix A. Supplementary data

Supplementary data to this article can be found online at https://doi.org/10.1016/j.eng.2019.02.003.

References

[1] Zhu Z, Lu Z, Wang D, Tang X, Yan Y, Shi W, et al. Construction of high-dispersed Ag/Fe$_3$O$_4$/g-C$_3$N$_4$ photocatalyst by selective photo-deposition and improved photocatalytic activity. Appl Catal B 2016;182:115–22.

[2] Di J, Xia J, Ji M, Wang B, Yin S, Zhang Q, et al. Advanced photocatalytic performance of graphene-like BN modified BiOBr flower-like materials for the removal of pollutants and mechanism insight. Appl Catal B 2016;183:254–62.

[3] Liu X, Steele JC, Meng XZ. Usage, residue, and human health risk of antibiotics in Chinese aquaculture: a review. Environ Pollut 2017;223:161–9.

[4] Li M, Liu Y, Liu S, Shu D, Zeng G, Hu X, et al. Cu(II)-influenced adsorption of ciprofloxacin from aqueous solutions by magnetic graphene oxide/nitrilotriacetic acid nanocomposite: competition and enhancement mechanisms. Chem Eng J 2017;319:219–28.

[5] Song Q, Fang Y, Liu Z, Li L, Wang Y, Liang J, et al. The performance of porous hexagonal BN in high adsorption capacity towards antibiotics pollutants from aqueous solution. Chem Eng J 2017;325:71–9.

[6] Wang J, He MF, Zhang D, Ren Z, Song T, Xie J. Simultaneous degradation of tetracycline by a microbial fuel cell and its toxicity evaluation by zebrafish. RSC Adv 2017;7(70):44226–33.

[7] Lei ZD, Wang JJ, Wang L, Yang XY, Xu G, Tang L. Efficient photocatalytic degradation of ibuprofen in aqueous solution using novel visible-light responsive graphene quantum dot/AgVO$_3$ nanoribbons. J Hazard Mater 2016;312:298–306.

[8] Han J, Zheng X, Zhang L, Fu H, Chen J. Removal of SO$_2$ on a nanoporous photoelectrode with simultaneous H$_2$ production. Environ Sci Nano 2017;4(4):834–42.

[9] Tang L, Wang J, Jia C, Lv G, Xu G, Li W, et al. Simulated solar driven catalytic degradation of psychiatric drug carbamazepine with binary BiVO$_4$ heterostructures sensitized by graphene quantum dots. Appl Catal B 2017;205:587–96.

[10] Liu N, Huang W, Zhang X, Tang L, Wang L, Wang Y, et al. Ultrathin graphene oxide encapsulated in uniform MIL-88A(Fe) for enhanced visible light-driven photodegradation of RhB. Appl Catal B 2018;221:119–28.

[11] Tang L, Jia C, Xue Y, Li L, Wang A, Xu G, et al. Fabrication of compressible and recyclable macroscopic g-C$_3$N$_4$/GO aerogel hybrids for visible-light harvesting: A promising strategy for water remediation. Appl Catal B 2017;219:241–8.

[12] Liu Z, Gao Z, Liu Y, Xia M, Wang R, Li N. Heterogeneous nanostructure based on 1T-phase MoS$_2$ for enhanced electrocatalytic hydrogen evolution. ACS Appl Mater Interfaces 2017;9(30):25291–7.

[13] Voiry D, Salehi M, Silva R, Fujita T, Chen M, Asefa T, et al. Conducting MoS$_2$ nanosheets as catalysts for hydrogen evolution reaction. Nano Lett 2013;13(12):6222–7.

[14] Jin X, Fan X, Tian J, Cheng R, Li M, Zhang L. MoS2 quantum dot decorated g-C$_3$N$_4$ composite photocatalyst with enhanced hydrogen evolution performance. RSC Adv 2016;6(58):52611–9.

[15] Liu X, Jiang L, Jiang X, Tian X, Huang Y, Hou P, et al. Design of superior ethanol gas sensor based on indium oxide/molybdenum disulfide nanocomposite via hydrothermal route. Appl Surf Sci 2018;447:49–56.

[16] Butler SZ, Hollen SM, Cao L, Cui Y, Gupta JA, Gutiérrez HR, et al. Progress, challenges, and opportunities in two-dimensional materials beyond graphene. ACS Nano 2013;7(4):2898–926.

[17] Gigot A, Fontana M, Serrapede M, Castellino M, Bianco S, Armandi M, et al. Mixed 1T–2H phase MoS$_2$/reduced graphene oxide as active electrode for enhanced supercapacitive performance. ACS Appl Mater Interfaces 2016;8(48):32842–52.

[18] Song Z, Liu W, Cheng N, Norouzi Banis M, Li X, Sun Q, et al. Origin of the high oxygen reduction reaction of nitrogen and sulfur co-doped MOF-derived nanocarbon electrocatalysts. Mater Horiz 2017;4(5):900–7.

[19] Liu S, Chen F, Li S, Peng X, Xiong Y. Enhanced photocatalytic conversion of greenhouse gas CO$_2$ into solar fuels over g-C$_3$N$_4$ nanotubes with decorated transparent ZIF-8 nanoclusters. Appl Catal B 2017;211:1–10.

[20] Cardoso JC, Stulp S, De Brito JF, Flor JBS, Frem RCG, Zanoni MVB. MOFs based on ZIF-8 deposited on TiO$_2$ nanotubes increase the surface adsorption of CO$_2$ and its photoelectrocatalytic reduction to alcohols in aqueous media. Appl Catal B 2018;225:563–73.

[21] Wan L, Shamsaei E, Easton CD, Yu D, Liang Y, Chen X, et al. ZIF-8 derived nitrogen-doped porous carbon/carbon nanotube composite for high-performance supercapacitor. Carbon 2017;121:330–6.

[22] Zhang Y, Lu Y, Feng S, Liu D, Ma Z, Wang S. On-site evolution of ultrafine ZnO nanoparticles from hollow metal–organic frameworks for advanced lithium ion battery anodes. J Mater Chem A Mater Energy Sustain 2017;5(43):22512–8.

[23] Lu X, Wang Y, Zhang X, Xu G, Wang D, Lv J, et al. NiS and MoS$_2$ nanosheet co-modified graphitic C$_3$N$_4$ ternary heterostructure for high efficient visible light photodegradation of antibiotic. J Hazard Mater 2018;341:10–9.

[24] Zhou C, Lai C, Xu P, Zeng G, Huang D, Li Z, et al. Rational design of carbon-doped carbon nitride/Bi$_{12}$O$_{17}$C$_{12}$ composites: a promising candidate photocatalyst for boosting visible-light-driven photocatalytic degradation of tetracycline. ACS Sustain Chem & Eng 2018;6(5):6941–9.

[25] Zhao K, Zhang X, Zhang L. The first BiOI-based solar cells. Electrochem Commun 2009;11(3):612–5.

[26] Wang D, Xiao Y, Luo X, Wu Z, Wang YJ, Fang B. Swollen ammoniated MoS$_2$ with 1T/2H hybrid phases for high-rate electrochemical energy storage. ACS Sustain Chem Eng 2017;5(3):2509–15.

[27] Zhang X, Liang Y. Nickel hydr(oxy)oxide nanoparticles on metallic MoS$_2$ nanosheets: a synergistic electrocatalyst for hydrogen evolution reaction. Adv Sci 2018;5(2):1700644.

[28] Wu D, Wang Y, Wang F, Wang H, An Y, Gao Z, et al. Oxygen-incorporated few-layer MoS$_2$ vertically aligned on three-dimensional graphene matrix for enhanced catalytic performances in quantum dot sensitized solar cells. Carbon 2017;123:756–66.

[29] Zeng X, Huang L, Wang C, Wang J, Li J, Luo X. Sonocrystallization of ZIF-8 on electrostatic spinning TiO$_2$ nanofibers surface with enhanced photocatalysis property through synergistic effect. ACS Appl Mater Interfaces 2016;8(31):20274–82.

[30] Hao X, Jin Z, Yang H, Lu G, Bi Y. Peculiar synergetic effect of MoS$_2$ quantum dots and graphene on metal-organic frameworks for photocatalytic hydrogen evolution. Appl Catal B 2017;210:45–56.

[31] Liang C, Li Z, Dai S. Mesoporous carbon materials: synthesis and modification. Angew Chem Int Ed 2008;47(20):3696–717.

[32] Hsiao MC, Chang CY, Niu LJ, Bai F, Li LJ, Shen HH, et al. Ultrathin 1T-phase MoS2 nanosheets decorated hollow carbon microspheres as highly efficient catalysts for solar energy harvesting and storage. J Power Sources 2017;345:156–64.

[33] Liu S, Wang J, Yu J. ZIF-8 derived bimodal carbon modified ZnO photocatalysts with enhanced photocatalytic CO$_2$ reduction performance. RSC Adv 2016;6(65):59998–60006.

[34] Liu S, Yu J, Mann S. Synergetic codoping in fluorinated Ti$_{1-x}$Zr$_x$O$_2$ hollow microspheres. J Phys Chem C 2009;113(24):10712–7.

[35] Liang P, Zhang C, Sun H, Liu S, Tade M, Wang S. Solar Photocatalytic water oxidation and purification on ZIF-8-derived C–N–ZnO composites. Energy Fuels 2017;31(3):2138–43.

[36] Zhang Y, Li Q, Liu C, Shan X, Chen X, Dai W, et al. The promoted effect of a metal–organic frameworks (ZIF-8) on Au/TiO$_2$ for CO oxidation at room temperature both in dark and under visible light irradiation. Appl Catal B 2018;224:283–94.

[37] Pramoda K, Kaur M, Gupta U, Rao CN. Nanocomposites of 2D-MoS$_2$ nanosheets with the metal-organic framework, ZIF-8. Dalton Trans 2016;45(35):13810–6.

[38] Sane PK, Tambat S, Sontakke S, Nemade P. Visible light removal of reactive dyes using CeO$_2$ synthesized by precipitation. J Environ Chem Eng 2018;6(4):4476–89.

[39] Huang W, Liu N, Zhang X, Wu M, Tang L. Metal organic framework g-C$_3$N$_4$/MIL-53(Fe) heterojunctions with enhanced photocatalytic activity for Cr(VI) reduction under visible light. Appl Surf Sci 2017;425:107–16.

[40] Huang G, Chen T, Chen W, Wang Z, Chang K, Ma L, et al. Graphene-like MoS$_2$/graphene composites: cationic surfactant-assisted hydrothermal synthesis and electrochemical reversible storage of lithium. Small 2013;9(21):3693–703.

[41] Saber MR, Khabiri G, Maarouf AA, Ulbricht M, Khalil ASG. A comparative study on the photocatalytic degradation of organic dyes using hybridized 1T/2H, 1T/3R and 2H MoS$_2$ nano-sheets. RSC Adv 2018;8(46):26364–70.

[42] Cui C, Wang Y, Liang D, Cui W, Hu H, Lu B, et al. Photo-assisted synthesis of Ag$_3$PO$_4$/reduced graphene oxide/Ag heterostructure photocatalyst with enhanced photocatalytic activity and stability under visible light. Appl Catal B 2014;158–159:150–60.

[43] Huang Y, Fan W, Long B, Li H, Zhao F, Liu Z, et al. Visible light Bi$_2$S$_3$/Bi$_2$O$_3$/Bi$_2$O$_2$CO$_3$ photocatalyst for effective degradation of organic pollutions. Appl Catal B 2016;185:68–76.

[44] Zhu Z, Yu Y, Dong H, Liu Z, Li C, Huo P, et al. Intercalation Effect of Attapulgite in g-C$_3$N$_4$ modified with Fe$_3$O$_4$ quantum dots to enhance photocatalytic activity for removing 2-mercaptobenzothiazole under visible light. ACS Sustain Chem Eng 2017;5(11):10614–23.

[45] Zhang C, Ai L, Jiang J. Graphene hybridized photoactive iron terephthalate with enhanced photocatalytic activity for the degradation of rhodamine B under visible light. Ind Eng Chem Res 2015;54(1):153–63.

[46] Wang J, Yu Y, Zhang L. Highly efficient photocatalytic removal of sodium pentachlorophenate with Bi$_3$O$_4$Br under visible light. Appl Catal B 2013;136–137:112–21.

[47] Jin X, Ye L, Wang H, Su Y, Xie H, Zhong Z, et al. Bismuth-rich strategy induced photocatalytic molecular oxygen activation properties of bismuth oxyhalogen: the case of Bi$_{24}$O$_{31}$C$_{l10}$. Appl Catal B 2015;165:668–75.

[48] Wang K, Zhang G, Li J, Li Y, Wu X. 0D/2D Z-scheme heterojunctions of bismuth tantalate quantum dots/ultrathin g-C$_3$N$_4$ nanosheets for highly efficient visible light photocatalytic degradation of antibiotics. ACS Appl Mater Interfaces 2017;9(50):43704–15.

[49] Li K, Zeng Z, Yan L, Luo S, Luo X, Huo M, et al. Fabrication of platinum-deposited carbon nitride nanotubes by a one-step solvothermal treatment strategy and their efficient visible-light photocatalytic activity. Appl Catal B 2015;165:428–37.

[50] Chen F, Yang Q, Wang Y, Yao F, Ma Y, Huang X, et al. Efficient construction of bismuth vanadate-based Z-scheme photocatalyst for simultaneous Cr(VI) reduction and ciprofloxacin oxidation under visible light: Kinetics, degradation pathways and mechanism. Chem Eng J 2018;348:157–70.

[51] Ou H, Ye J, Ma S, Wei C, Gao N, He J. Degradation of ciprofloxacin by UV and UV/H$_2$O$_2$ via multiple-wavelength ultraviolet light-emitting diodes: effectiveness, intermediates and antibacterial activity. Chem Eng J 2016;289:391–401.

[52] Deng J, Ge Y, Tan C, Wang H, Li Q, Zhou S, et al. Degradation of ciprofloxacin using α-MnO$_2$ activated peroxymonosulfate process: effect of water constituents, degradation intermediates and toxicity evaluation. Chem Eng J 2017;330:1390–400.

[53] Paul T, Dodd MC, Strathmann TJ. Photolytic and photocatalytic decomposition of aqueous ciprofloxacin: transformation products and residual antibacterial activity. Water Res 2010;44(10):3121–32.

[54] Wei X, Chen J, Xie Q, Zhang S, Ge L, Qiao X. Distinct photolytic mechanisms and products for different dissociation species of ciprofloxacin. Environ Sci Technol 2013;47(9):4284–90.

[55] Ao X, Liu W, Sun W, Cai M, Ye Z, Yang C, et al. Medium pressure UV-activated peroxymonosulfate for ciprofloxacin degradation: kinetics, mechanism, and genotoxicity. Chem Eng J 2018;345:87–97.

[56] Deng Y, Tang L, Zeng G, Wang J, Zhou Y, Wang J, et al. Facile fabrication of mediator-free Z-scheme photocatalyst of phosphorous-doped ultrathin graphitic carbon nitride nanosheets and bismuth vanadate composites with enhanced tetracycline degradation under visible light. J Colloid Interface Sci 2018;509:219–34.

[57] Barhoumi N, Olvera-Vargas H, Oturan N, Huguenot D, Gadri A, Ammar S, et al. Kinetics of oxidative degradation/mineralization pathways of the antibiotic tetracycline by the novel heterogeneous electro-Fenton process with solid catalyst chalcopyrite. Appl Catal B 2017;209:637–47.

[58] Zhu Z, Yu Y, Huang H, Yao X, Dong H, Liu Z, et al. Microwave-hydrothermal synthesis of a novel, recyclable and stable photocatalytic nanoreactor for recognition and degradation of tetracycline. Catal Sci Technol 2017;7 (18):4092–104.

[59] Yang Y, Zeng Z, Zhang C, Huang D, Zeng G, Xiao R, et al. Construction of iodine vacancy-rich BiOI/Ag@AgI Z-scheme heterojunction photocatalysts for visible-light-driven tetracycline degradation: transformation pathways and mechanism insight. Chem Eng J 2018;349:808–21.